

Mid-Infrared diagnostics of metal-rich H II regions from VLT and *Spitzer* Spectroscopy of Young Massive Stars in W31^{*}

J. P. Furness¹, P. A. Crowther^{1†}, P. W. Morris², C. L. Barbosa³, R. D. Blum⁴,
P. S. Conti⁵, S. D. van Dyk⁶

¹*Department of Physics and Astronomy, University of Sheffield, Sheffield S3 7RH, UK*

²*NASA Herschel Science Center/CalTech, 220-6, Pasadena, CA 91125, USA*

³*IP&D, Universidade do vale do Paraíba, Av. Shishima Hifumi, 2911, São José dos Campos 12244-000, SP, Brazil*

⁴*NOAO, 950 North Cherry Avenue, Tucson, AZ 85719, USA*

⁵*JILA, University of Colorado, Boulder, CO 80309-0440, USA*

⁶*Spitzer Science Center/CalTech, 220-6, Pasadena, CA 91125, USA*

13 December 2009

ABSTRACT

We present near-IR VLT/ISAAC and mid-IR *Spitzer*/IRS spectroscopy of the young massive cluster in the W31 star-forming region. *H*-band spectroscopy provides refined classifications for four cluster members O stars with respect to Blum et al. In addition, photospheric features are detected in the massive Young Stellar Object (mYSO) #26. Spectroscopy permits estimates of stellar temperatures and masses, from which a cluster age of ~ 0.6 Myr and distance of 3.3 kpc are obtained, in excellent agreement with Blum et al. IRS spectroscopy reveals mid-infrared fine structure line fluxes of [Ne II-III] and [S III-IV] for four O stars and five mYSOs. In common with previous studies, stellar temperatures of individual stars are severely underestimated from the observed ratios of fine-structure lines, despite the use of contemporary stellar atmosphere and photoionization models. We construct empirical temperature calibrations based upon the W31 cluster stars of known spectral type, supplemented by two inner Milky Way ultracompact (UC) H II regions whose ionizing star properties are established. Calibrations involving [Ne III] $15.5\mu\text{m}$ /[Ne II] $12.8\mu\text{m}$, [S IV] $10.5\mu\text{m}$ /[Ne II] $12.8\mu\text{m}$ or [Ar III] $9.0\mu\text{m}$ /[Ne II] $12.8\mu\text{m}$ have application in deducing the spectral types of early- to mid-O stars for other inner Milky Way compact and UC H II regions. Finally, evolutionary phases and timescales for the massive stellar content in W31 are discussed, due to the presence of numerous young massive stars at different formation phases in a ‘coeval’ cluster.

Key words: (Galaxy:) open clusters and associations: individual: W31 (G10.2–0.3) – (ISM:) H II regions – Stars: early-type; – Stars: fundamental parameters – Infrared: ISM

1 INTRODUCTION

The formation of high mass stars remains an unsolved astrophysical puzzle (Zinnecker & Yorke 2007; Clarke & Bonnell 2008). Unlike the situation for low mass stars, for

which multiwavelength observations are plentiful, very massive stars ($M_* \geq 25M_\odot$) are born within compact, deeply embedded star-forming regions, severely restricting observations to either the far-infrared where heated dust dominates their appearance, or radio wavelengths where gas ionized by the central star(s) can be characterised. Either way, high mass stars themselves cannot be seen directly within these ultracompact (UC) H II regions (Churchwell 2002) until the column density of dust along our line of sight falls below 2–4 magnitudes in the *K*-band. To date, only a few such cases have been identified – G23.96+0.15 (Hanson, Luhman & Rieke 2002;

^{*} Based on observations made with ESO telescopes at the Paranal Observatory under programme ID 077.C-0550(A) and the Spitzer Space Telescope which is operated by the Jet Propulsion Laboratory, California Institute of Technology under NASA contract 1407

[†] Paul.Crowther@shef.ac.uk

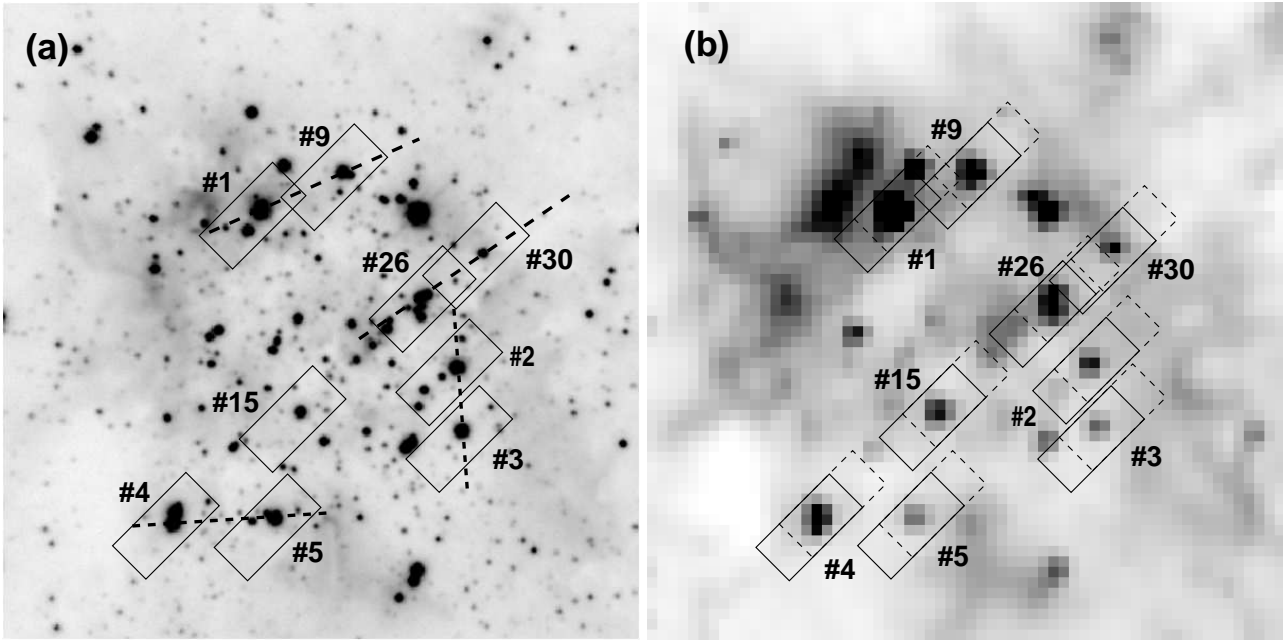


Figure 1. (a) K -band image of W31 from Blum et al. (2001), showing the 4 slit positions for the near-IR ISAAC spectroscopy (dashed lines) and the 9 IRS apertures for the first nod position of the mid-IR spectroscopy. North is up, East to the left and the image is $72'' \times 72''$ or 1.2×1.2 pc at our adopted distance of 3.3 kpc; (b) $3.6\mu\text{m}$ IRAC image of W31 showing both IRS nod positions (first solid; second dotted) at the same scale and orientation as for (a).

Crowther & Furness 2008), G29.96–0.02 (Watson & Hanson 1997; Hanson et al. 2005), G45.45+0.06 (Blum & McGregor 2008), W51d (Barbosa et al. 2008) – with the stellar content of other UC H II regions reliant upon indirect far-IR or radio continuum techniques (Wood & Churchwell 1989; Kurtz et al. 1994).

Fortunately, the advent of efficient mid-infrared imaging and spectroscopy from space with *Infrared Space Observatory* (ISO, Kessler et al. 1996) and *Spitzer* (Werner et al. 2004), plus ground-based 8–10m telescopes has opened up a further window to study such embedded regions. Specifically, a number of fine-structure lines from ionized regions are seen in the mid-infrared, notably [Ne II–III], [S III–IV], which albeit indirect, provide information upon the hardness of the extreme ultraviolet (EUV) radiation from their constituent O stars. Such diagnostics, analogous to the optical forbidden lines of [O II–III] and [S II–III], may allow the ‘inverse problem’ of establishing properties of the ionizing stars of ultra-compact and compact H II regions (see Okamoto et al. 2003). Alternatively, indirect approaches based upon near-IR hydrogen and helium nebular lines are also employed (e.g. Lumsden et al. 2003; Blum & McGregor 2009).

To date, tests of photoionization and stellar atmosphere models using these mid-IR line diagnostics have been rather unsatisfactory. Firstly, this is because H II regions are usually ionized by multiple early-type stars in compact clusters, and secondly the strength of mid-IR fine structure lines is affected both by the energetic photons from OB stars and nebular properties. The most comprehensive study of a UC H II region attempted to date has been by Morisset et al. (2002) for G29.96–0.02 whose results suggested a temperature of $T_{\text{eff}} \sim 35 \pm 3\text{ kK}$ for the ionizing star, in contrast to $T_{\text{eff}} \sim 41 \pm 2\text{ kK}$ from a non-LTE analysis of near-IR spectroscopy for the star (Hanson, Puls & Repolust 2005).

Photoionization models are widely used to infer the stellar properties of both embedded H II regions (Sellmaier et al. 1996; Giveon et al. 2002; Simón-Díaz & Stasińska 2008; Pérez-Montero & Vílchez 2009) and entire galaxies from mid-IR fine structure lines (Lutz et al. 1996; Rigby & Rieke 2004). If the highly discrepant effective temperatures obtained for G29.96–0.02 using indirect techniques were repeated for other, single, embedded O stars, then previously published results from mid-IR diagnostics may be called into question, especially those at high metallicity (e.g. Thornley et al. 2000).

The focus of the present study is the Galactic Giant H II region (GHR) W31, specifically the young star cluster (10.2–0.3, hereafter W31) discussed by Blum, Daminieli & Conti (2001). This cluster, for which Blum et al. (2001) established a distance of 3.4 kpc and extinction of $A_K = 1.7$ mag, hosts a minimum of four ‘naked’ O-type stars, as deduced from near-IR spectroscopy, plus a number of massive stars which are still embedded at near-IR wavelengths (hereafter massive YSOs) plus numerous UC H II regions (Ghosh et al. 1989). As such, this cluster provides an excellent opportunity to study the different early evolutionary phases of massive star formation. In addition, it possesses an unusual morphology, in that the highest mass stars are located at the periphery of the cluster, in contrast to the mass segregated morphology of most other young clusters (de Grijs et al. 2002; Allison et al. 2009). We shall exploit this unusual geometry through spectroscopy of individual early-type stars in W31 with the Infrared Spectrograph (IRS, Houck et al. 2004) aboard *Spitzer*, supplemented with H and K band VLT observations with the Infrared Spectrograph and Array Camera (ISAAC, Moorwood & Cuby 1998).

Our aim is to compare photoionization model predictions of individual H II regions with stellar temperatures

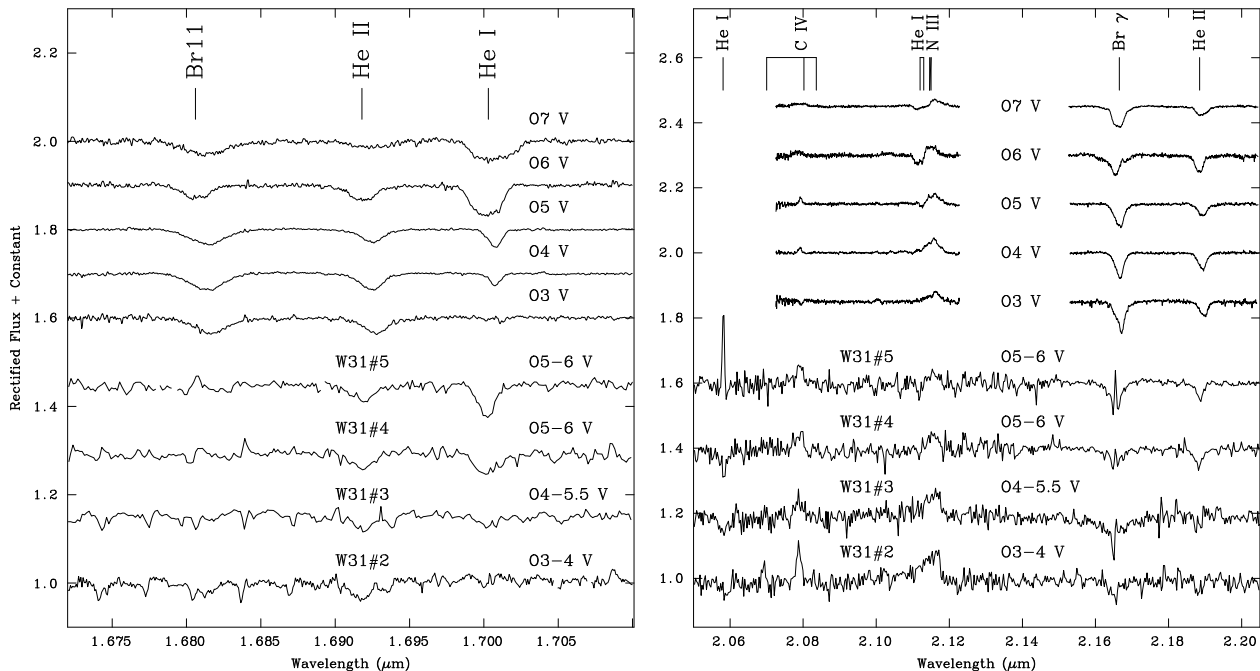


Figure 2. *H* band (left panel) and *K* band (right panel) VLT/ISAAC spectra of the O stars in W31, plus template stars from Hanson et al. (2005). All stars show stellar absorption of He II and He I in the *H* band, the ratio of which we use to spectral type the stars. The stars also show C IV and N III emission in the *K*-band indicating early-mid type O stars. The later of the O stars also show Br γ emission, indicating a younger evolutionary phase where more nebula material is present around the star.

obtained directly from near-IR spectroscopic analysis. We are thus able to significantly increase the statistics of H II regions for which mid-IR diagnostics are available, whose ionizing stars are well constrained. Our results are of potential application in deducing ionizing stars of UC H II regions within the inner Milky Way based upon fine structure diagnostics available from ground-based telescopes, namely [S IV] $10.5\mu\text{m}$ and [Ne II] $12.8\mu\text{m}$ (Zhu et al. 2008). The diffraction limit of 8–10m telescopes in the N-band is ~ 0.4 arcsec, equivalent to a physical scale of 0.01 pc at a distance of 5 kpc, well below the 0.1 pc size of typical UC H II regions (Okamoto et al. 2003).

The present paper is structured as follows. § 2 detail the VLT and *Spitzer* observations, while §3 presents refined spectral classification of naked O stars in W31. § 4 presents the mid-IR fine structure lines from W31 sources, including predictions from photoionization models and empirical calibrations. A discussion of mid-IR fine structure lines is presented § 5 together with the massive star content of W31. Brief conclusions are drawn in § 6.

2 OBSERVATIONS AND DATA REDUCTION

Two main observational datasets are used in the present study, obtained with the VLT ISAAC near-IR spectrograph and *Spitzer* IRS mid-IR spectrograph.

2.1 VLT ISAAC spectroscopy

Long-slit *H*- and *K*-band near-infrared spectroscopy of sources in W31 were obtained with the ISAAC instrument

mounted at the Very Large Telescope between 4th April–17th June 2006 (Programme 077.C-0550(A), P.I. Crowther). Four slit positions were used, as illustrated in Fig. 1(a). Each included two or more targets of interest, namely the naked O stars and massive YSO’s from Blum et al. (2001).

The detector was the 1024×1024 Hawaii Rockwell array, while three medium resolution grating settings ($0.775\text{\AA}/\text{pixel}$) were obtained, centred at 1.71 , 2.09 and $2.20\mu\text{m}$. These observations were obtained at low airmass during variable seeing conditions using a 0.6 arcsec wide slit, and reduced using standard IRAF packages. We observed using ABBA nod-cycles, a standard infrared A number of AB pairs were obtained for each grating setting with wavelength solutions achieved from comparison XeAr arc images. From these, the observations covered $1.671\text{--}1.751\mu\text{m}$, $2.029\text{--}2.155\mu\text{m}$ and $2.140\text{--}2.265\mu\text{m}$ at spectral resolutions of 3.8\AA , 6.0\AA and 6.0\AA respectively, as measured from arc lines.

Telluric correction was achieved by spectroscopy of early-G dwarfs observed at similar airmass to W31, corrected for their spectral features using high resolution observations of the Sun, adjusted for the radial velocity and spectral resolution of the template stars. An extensive discussion of telluric correction for medium resolution near-IR spectroscopy of early-type stars is provided by Hanson et al. (2005). The $2.09\mu\text{m}$ setup suffered from low-level variable structure which was accentuated upon flat-fielding, arising from a 50 Hz pickup inherent to the instrument. Only the two other settings were flat-fielded. Consequently, the continuum S/N achieved was lower for this grating position (~ 100) than the other settings (~ 200).

Table 1. Classification of early-type stars in W31 from VLT/ISAAC spectroscopy based upon the near-IR calibration of Crowther & Furness (2008).

	EW (Å)		$\log \frac{\text{He II}}{\text{He I}}$	Spectral Type		
	He II (1.692 μm)	He I (1.700 μm)		This Work	Blum et al.	Further Comments
#2	0.59 ± 0.08	< 0.2	$> 0.47 \pm 0.06$	O3–4 V	O5.5 V	N III, C IV in emission
#3	0.40 ± 0.08	0.27 ± 0.07	0.17 ± 0.20	O5 $_{-1}^{+0.5}$ V	O5.5 V	N III, C IV in emission
#4	0.58 ± 0.06	0.87 ± 0.06	-0.17 ± 0.07	O5.5 ± 0.5 V	O5.5 V	N III, C IV in emission
#5	0.68 ± 0.05	0.96 ± 0.04	-0.15 ± 0.05	O5.5 ± 0.5 V	O5.5 V	N III, C IV in emission, nebular emission from Br γ , He I 2.058 μm

2.2 Spitzer IRS spectroscopy

W31 was observed with the mid-IR spectrograph IRS in GO #3337 (W31CLUST, P.I. Crowther) between 14–16 September 2005 using all four modules, sampling the short wavelength region at low and high resolution (SL and SH), plus the long wavelength region at low and high resolution (LL and LH). In addition, W31 was imaged with the IRAC instrument (Fazio et al. 2004) at 3.6, 4.8, 5.8 and 8.0 μm , using HDR mode, with 12 s exposures in a 12 position, Reuleaux dither pattern. Unfortunately, the IRAC 5.8 and 8.0 μm imaging and long wavelength IRS observations were heavily saturated, so our analysis largely focuses upon the SH, staring mode (30 sec, 6 cycles) observation with IRS, obtained at two nod positions. The spectral range covered was 9.9–19.6 μm , at a resolution of $R \sim 600$.

The individual $4.7 \times 11.3 \text{ arcsec}^2$ ($2 \times 5 \text{ pix}$) apertures from the first nod position are superimposed upon a K -band image of W31 in the Fig 1(a). Fig 1(b) shows both IRS nod positions together with the IRAC 3.6 μm image of W31. A background subtraction was applied to these two dimensional IRS datasets – prior to extraction – using a dedicated OFF position at 18:09:30.4 –20:20:00 (J2000) from a second set of cluster positions which are not presented in this paper. This pointing gives a correction for nebular emission in the extended H II region, including the PAH’s. However, it does not correct for emission from the dense material close to each of the targeted stars.

Observations have been processed and calibrated in the standard IRS pipeline to basic calibrated data products (BCDs), using a version which is compatible with S16.2. Multiple exposures at the same position have been co-added at the BCD (2 dimensional) level, and the OFF position has been used to correct rogue pixels and subtract the extended background. Then the spectra were extracted with the offline S16.2 post-BCD pipeline. Spectra from the two staring-mode nods were averaged, except for cases for which a single nod was used to minimise contamination. Specifically, only nod 1 was used for #1 and #26 and only nod 2 was used for #2 and #30. This is to avoid contamination from potentially interloping sources during extraction of the spectra (recall Fig. 1(b)). These sources are identified within the nods from any of the available imaging observations, including unsaturated regions of the IRAC datasets.

Since the width of the full width at half maximum of the central Airy pattern of the IRS point source function is comparable to the size of the SH slit itself, the full slit is extracted, so it is not possible to extract (or even easily identify) separate sources or the background.

Each of the echelle spectral orders were trimmed at the red edges, corresponding to the lower part of the array where photometric response sharply drops. Final spectra have been created by merging the orders into single spectra, with excellent inter-order agreement when the point-source flux calibration is applied, with only minor offsets (well within the photometric uncertainties of 15%), indicating that the dominant source signal from each of the intended targets behave more consistently as point sources than extended sources. Formally, a 1σ absolute flux calibration of 10% was achieved, except for the raw 18.7 μm [S III] line which was saturated in a few cases. These were corrected by linearization and extrapolation, from which an additional 5% uncertainty resulted.

Finally, we should note that these observations have been obtained when the SH array was relatively undamaged by the cumulative effects of space weather, thus receive good correction for rogue pixels with data at the OFF position. Furthermore, these observations are not affected in the calibrations or data quality by more recent versions of the pipelines (through S18.x) which mainly benefit the IRS peak up imaging AOT and data obtained with more aged arrays.

3 PROPERTIES OF EARLY-TYPE STARS IN W31 FROM NEAR-IR SPECTROSCOPY

3.1 Near-IR classification of W31 O stars

In Figure 2 we present our H - and K -band ISAAC spectroscopy of naked O stars in W31, together with spectra of template O stars from the high resolution atlas of Hanson et al. (2005). Crowther & Furness (2008) have recently presented a method of determining O dwarf subtypes from the ratio of the observed He II 1.692 μm to He I 1.700 μm equivalent widths. These were measured from the emission line fitting (ELF) suite of routines in the STARLINK spectroscopic analysis programme DIPSO and are presented in Table 1 together with inferred spectral types.

Stars #3, #4 and #5 all show clear He I and He II absorption features, from which O5 $_{-1}^{+0.5}$ V, O5.5 ± 0.5 V and O5.5 ± 0.5 V classifications are obtained, according to Fig. 3 of Crowther & Furness (2008), in close agreement with Blum et al. (2001). K -band spectroscopy reveals C IV, N III emission features, plus Br γ and He II 2.189 μm absorption, the core of the former filled-in by nebular Br γ emission.

In the case of #2, negligible He I 1.700 μm is observed, from which an O3–4 V classification is inferred. If we had

Table 2. Interstellar extinctions, A_K , and distance modulus (DM) towards individual stars in W31 using near-IR photometry of Blum et al. (2001) and the absolute magnitude calibration of Martins & Plez (2006)

W31 #	m_K mag	$H - K$ mag	$(H - K)_0$ mag	E_{H-K} mag	A_K mag	M_K mag	DM
2	10.02	1.16	-0.10	1.26	2.29	-4.98	12.71
3	10.30	1.06	-0.10	1.16	2.11	-4.39	12.58
4	10.34	0.88	-0.10	0.98	1.78	-4.27	12.83
5	10.37	1.26	-0.10	1.36	2.47	-4.27	12.17
Average					2.16		12.57
σ					0.29		0.29

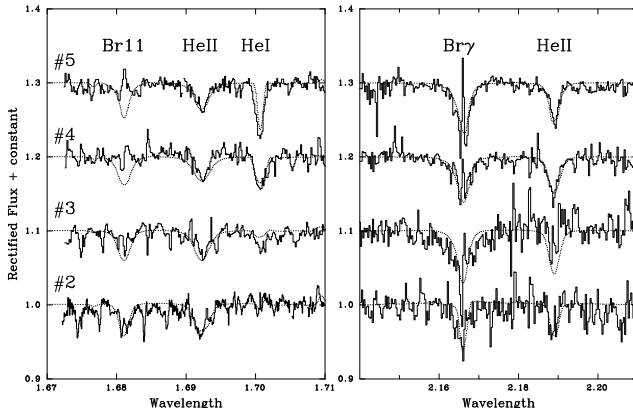


Figure 3. H -band and K -band spectroscopic fits (dotted lines) to VLT/ISAAC (solid lines) observations of hydrogen and helium lines in W31 #2 (O3–4 V), #3 ($O5^{+0.5}_{-1}$ V), #4 ($O5.5 \pm 0.5$ V) and #5 ($O5.5 \pm 0.5$ V).

classified #2 on the basis of its K -band spectrum, the presence of significant C IV emission would have suggested a spectral type of O4V or later (Hanson et al. 2005).

3.2 Distance and Age of W31

Armed with our refined spectral types, we now use the near-IR photometry from Blum et al. (2001) and observational absolute magnitude calibration of Martins & Plez (2006) to obtain a revised distance to W31. This is presented in Table 2, in which observed colours of O stars pro-

Table 3. Stellar properties of the W31 O stars from non-LTE CMFGEN models using a distance of 3.3 kpc. Uncertainties in stellar temperatures are ± 1.5 kK, with the exception of #2 for which an upper limit is 48 kK. Current stellar masses are obtained from comparison with $2 \times Z_\odot$ theoretical isochrones from Lejeune & Schaerer (2001).

W31 #	Sp. Type	T_{eff} kK	$\log L$ L_\odot	$\log \dot{M}$ $M_\odot \text{yr}^{-1}$	$\log g$ cgs	$v \sin i$ km s^{-1}	M M_\odot	M_K mag
2	O3–4 V	45	5.79	-5.5	4.00	100	61	-4.84
3	$O5^{+0.5}_{-1}$ V	43	5.56	-5.8	4.04	200	46	-4.38
4	$O5.5 \pm 0.5$ V	41	5.36	-6.1	4.04	200	36	-4.01
5	$O5.5 \pm 0.5$ V	41	5.62	-5.9	3.94	100	45	-4.67

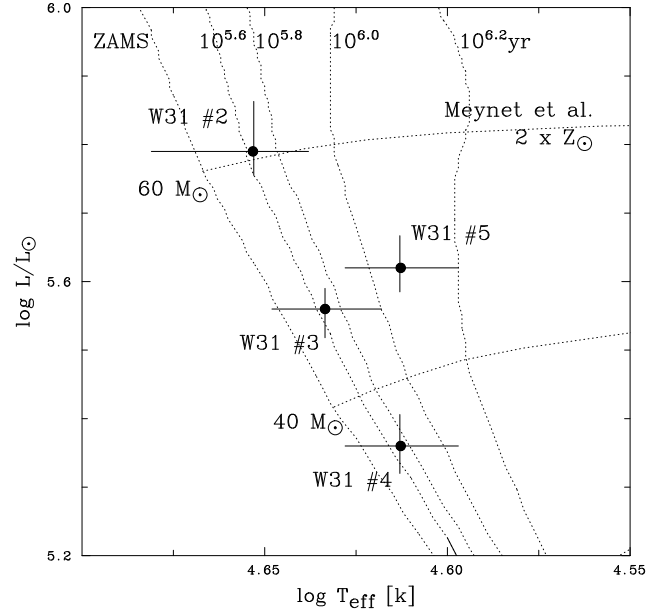


Figure 4. Hertzsprung-Russell diagram of the 4 naked O stars in W31. Lejeune & Schaerer (2001) isochrones are shown for ages of 10^3 , $10^{5.6}$, $10^{5.8}$, $10^{6.0}$ and $10^{6.2}$ yr, based on the $2 \times Z_\odot$ Meynet et al. (1994) evolutionary tracks, from which a cluster age of ~ 0.6 Myr is obtained.

vide a direct measurement of interstellar extinction from $A_K \sim 1.82 E_{H-K}$ from Indebetouw et al. (2005). For #4 and #5 uncertainties in subtypes have little influence upon absolute magnitudes, while subtype uncertainties formally introduce absolute magnitude uncertainties of up to 0.3 mag for #2 and #3. These are mitigated somewhat by the typical spread of ± 0.5 mag in absolute magnitudes for individual spectral types.

Overall, we obtain a higher interstellar extinction of $A_K = 2.16 \pm 0.29$ mag towards W31 than Blum et al. (2001) on the basis of updated intrinsic colours, but this is largely cancelled out by the revised absolute magnitude calibration. As such, we obtain a very similar overall distance ($3.3^{+0.4}_{-0.3}$ kpc) to the 3.4 kpc distance obtained by Blum et al. (2001).

For an adopted Galactic Centre distance of 8.0 kpc (Reid 1993) for the Sun, our preferred distance to W31 suggests that it lies ~ 4.8 kpc from the Galactic Centre. The Galactic oxygen metallicity gradient is $\Delta \log (O/H) = -0.044 \pm 0.010 \text{ dex kpc}^{-1}$ (Esteban et al. 2005), from which we anticipate that W31 is 40% more metal-rich than H II regions within the Solar circle, i.e. $\log O/H + 12 \sim 8.81$, compared to 8.65 for the Orion Nebula at a Galactocentric distance of ~ 8.4 kpc (Esteban et al. 2005; Simón-Díaz et al. 2006). We are unable to derive a neon or sulphur abundance for W31 from the IRS spectroscopy since the nebular electron temperature is unknown.

Having established a slightly refined cluster distance, we now estimate stellar temperatures (and in turn luminosities) from spectroscopic fits to the near-IR diagnostics with the non-LTE CMFGEN code of Hillier & Miller (1998). CMFGEN solves the radiative transfer equation in the co-moving frame, under the additional constraint of statistical equilibrium. Since CMFGEN does not solve the momentum equation, a density or velocity structure is required. For the

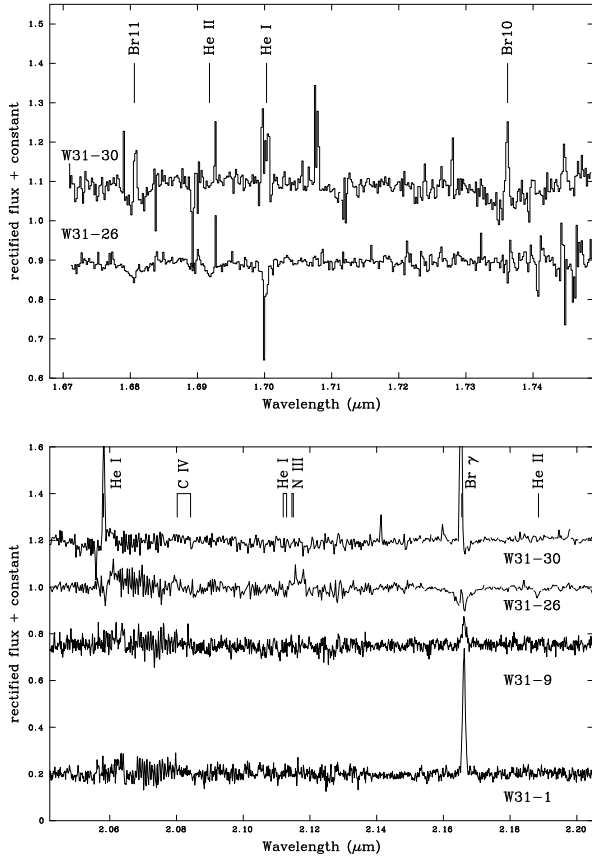


Figure 5. *H* band (top panel) and *K* band (lower panel) VLT/ISAAC spectra of the massive YSOs in W31. No *H* band spectra are available for W31 #1 and #9. $\text{Br}\gamma$ is seen in emission throughout, while underlying photospheric absorption is also seen in #26, demonstrating an evolutionary phase between the embedded and naked O star phases.

supersonic part, the velocity is parameterized with a classical β -type law, with an exponent of $\beta=1$ adopted. This is connected to a hydrostatic density structure at depth, such that the velocity and velocity gradient match at the interface. The subsonic velocity structure is set by a corresponding fully line-blanketed plane-parallel TLUSTY model (v.200, see Lanz & Hubeny 2003). The atomic model is similar to that adopted in Hillier et al. (2003), including ions from H, He, C, N, O, Ne, Si, S, Ar, Ca and Fe, with metal abundances increased by a factor of two relative to those of the Sun from Asplund et al. (2004) for O, Ne and Ar, or Cox (2000) otherwise.

We have assumed a depth-independent Doppler profile for all lines when solving for the atmospheric structure in the co-moving frame, while in the final calculation of the emergent spectrum in the observer's frame, we have adopted a uniform turbulence of 50 km s^{-1} . Incoherent electron scattering and Stark broadening for hydrogen and helium lines are adopted. Finally, we convolve our synthetic spectrum with a rotational broadening profile. In view of the quality of our observations, rotational velocities should be reliable to $\pm 50 \text{ km s}^{-1}$.

For an adopted (uniform) terminal wind velocity of 2000

km s^{-1} , surface gravity of $\log g = 4$ and abundance ratio of $\text{He}/\text{H}=0.1$ by number, we varied the stellar radius and (non-clumped) mass-loss rate until an acceptable match to the $\text{He II } 1.692\mu\text{m}$, $\text{He I } 1.700\mu\text{m}$, $\text{Br}\gamma$ and $\text{He II } 2.189\mu\text{m}$ was achieved. For the case of #2 (O3–4 V), for which negligible $\text{He I } 1.700\mu\text{m}$ absorption is detected, we favour a temperature of $\sim 45 \text{ kK}$ since higher temperatures produce too weak $\text{Br}\gamma$ absorption. Spectroscopic fits are presented in Fig. 3 while resulting physical and wind properties are shown in Table 3. Fits to diagnostic lines are generally satisfactory with the exception of #3 for which $\text{He II } 2.189\mu\text{m}$ suffers from low S/N, such that we rely upon the weaker $1.692\mu\text{m}$ line in this instance. Note that prominent nebular emission features are seen in the hydrogen Brackett series, with the possible exception of #2.

Our spectroscopic analysis did not yield a precise measurement of surface gravities (and in turn masses), so having established temperatures and luminosities, we overplot $2\times Z_{\odot}$ theoretical isochrones from Lejeune & Schaerer (2001) in Figure 4, from which an age of $\sim 0.6 \text{ Myr}$ was obtained, together with corresponding surface gravities and mass estimates (see Table 3). Three of the four O stars lie along a common isochrone of $\sim 0.5 \text{ Myr}$, although from Fig. 4 #5 suggests a greater age of $\geq 1 \text{ Myr}$. However, it is possible that this source is a close double with equal mass components, whose absolute magnitudes would have $M_K = -3.9 \text{ mag}$ for a distance of 3.3 kpc. In this case, individual components would have properties similar to those of #4 in Table 3, reducing the inferred cluster age to $\sim 0.5 \text{ Myr}$.

3.3 Near-IR spectroscopy of massive YSOs

In addition to the naked O stars, we have obtained ISAAC spectroscopy of four massive YSOs in W31 - high mass stars whose photospheric features are veiled by circumstellar dust with IR excesses due to hot dust. We observed #1, #9, #26 and #30 from Blum et al. (2001) at both grating settings in the *K*-band spectra, but only #26 and #30 were observed in the *H*-band. These datasets are shown in Figure 5. In general, our observations confirm the lower quality datasets of Blum et al. (2001), with nebular Brackett emission lines, plus nebular $\text{He I } 1.700, 2.058\mu\text{m}$ for #30.

Uniquely among the massive YSOs, #26 shows clear photospheric $\text{Br}\gamma$ absorption in addition to weak nebular $\text{Br}\gamma$ emission, plus $\text{He II } 2.189\mu\text{m}$, $1.692\mu\text{m}$ and $\text{He I } 1.700\mu\text{m}$ absorption. From the observed *H*-band classification diagnostics in the *H*-band we estimate an approximate spectral type of O6, since $\log W_{\lambda}(\text{He II } 1.692)/W_{\lambda}(\text{He I } 1.700) \sim -0.26$. This star appears to be at the point of revealing its photosphere, despite the presence of a strong IR dust excess ($H - K = 2.72 \text{ mag}$ from Blum et al. 2001).

In principle, we could estimate the physical properties of #26, by combining an estimate of its stellar temperature ($\sim 36 \text{ kK}$) with the *H*-band photometry from Blum et al. (2001), the mean *H*-band extinction for the naked O stars ($A_H \sim 3.4 \text{ mag}$) and the adopted distance of 3.3 kpc. For this star the *H*-band is selected on the basis of significant dust emission in the *K*-band. Unfortunately, the resulting parameters for #26 are unphysical since $\log L/L_{\odot} = 4.2$ would be obtained, i.e. mass of only $4M_{\odot}$ (!) for an assumed surface gravity of $\log g = 4.0$. More plausibly, #26 may possess a small dust excess, i.e. a large colour excess due to extreme

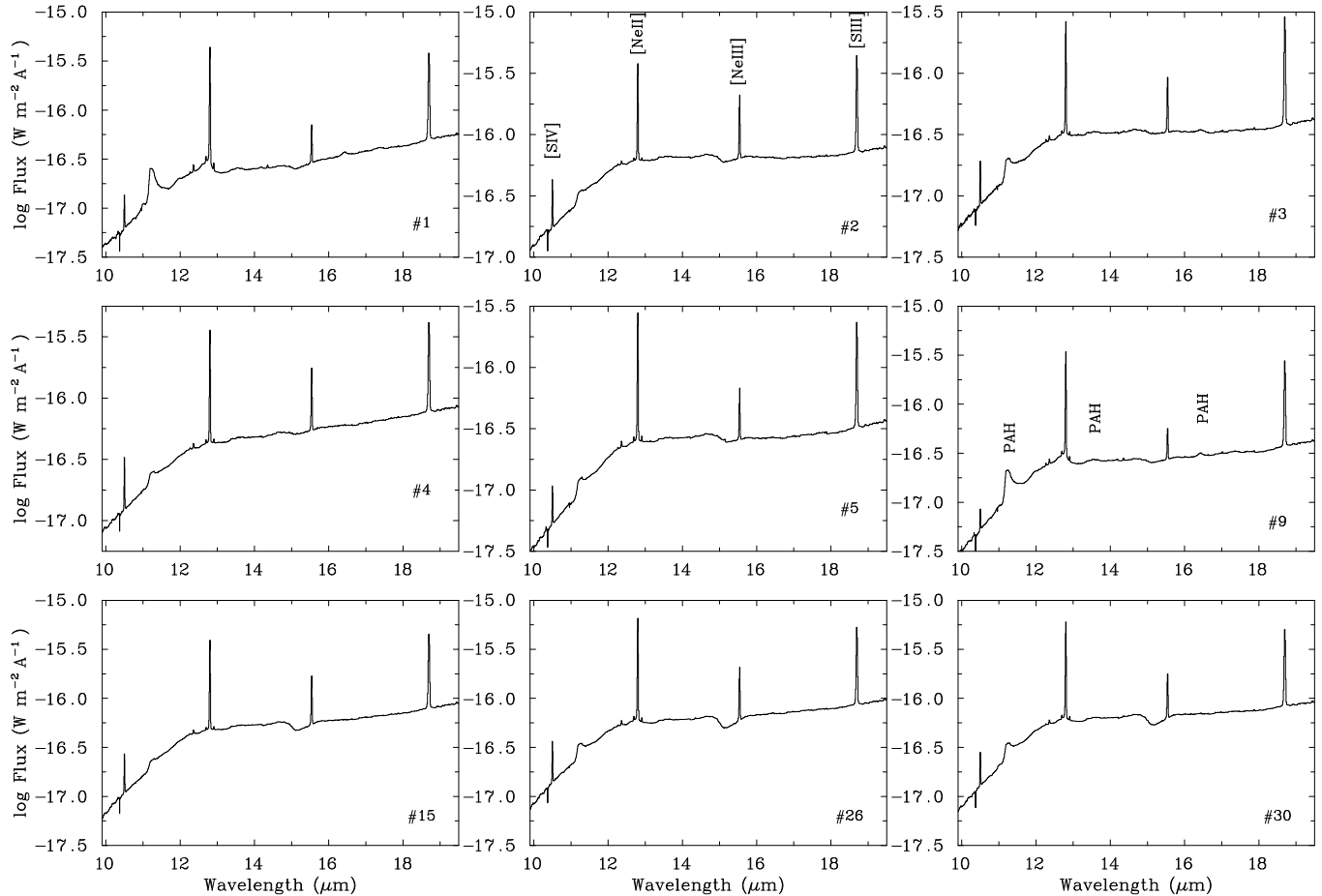


Figure 6. IRS short high (SH) medium resolution spectroscopy of W31 sources, for which the fine structure lines of [S IV], [Ne II], [Ne III] and [S III] are indicated in #2, and the PAH (UIR) features are marked in #9. These mid-IR datasets have been background subtracted using an OFF pointing.

extinction. Recall that this source lies close to the reddening line in the colour-magnitude diagram (Blum et al. 2001). If the $(H - K)$ color were to arise solely from line-of-sight extinction, $A_H \sim 7.9$ mag, from which $\log L/L_\odot = 6.2$ would be obtained. In reality, the physical properties of #26 will lie between these two extreme cases. Regardless, this star warrants further study since it uniquely displays both stellar and circumstellar features amongst early-type stars in W31.

4 INDIRECT PROPERTIES OF EARLY-TYPE STARS IN W31 FROM IRS SPECTROSCOPY

4.1 Mid-IR fine structure line ratios

We present the *Spitzer* IRS short high medium resolution observations of the naked O stars and massive YSOs in Fig 6. Although these datasets are background subtracted, no allowance for extended nebular emission close to each source is made. Their continua are dominated by warm dust emission, while the solid state Polycyclic Aromatic Hydrocarbon (PAH) features at $11.3\mu\text{m}$, $13.6\mu\text{m}$ and $16.5\mu\text{m}$ – previously known as Unidentified Infrared (UIR) emission – are also seen (the $16.5\mu\text{m}$ PAH feature is not detected in #2). There is also a tentative detection of $15.2\mu\text{m}$ ab-

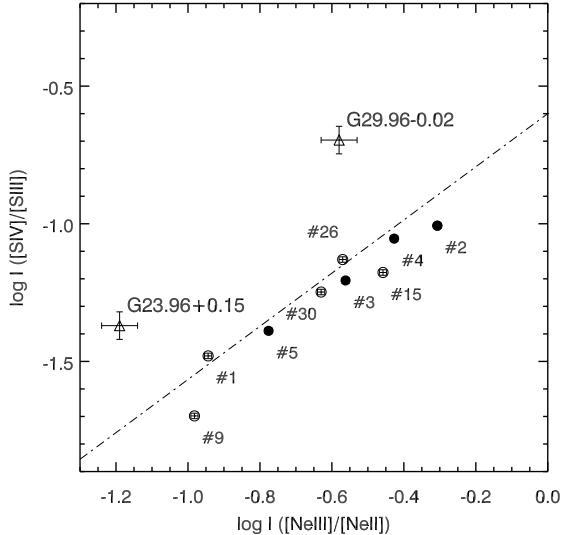
sorption by icy CO_2 mantles on the silicate dust grains (van Dishoeck 2004). Shallow profiles with a soft blue wing starting near $14.9\mu\text{m}$ are reminiscent of the W33A massive YSO (Gibb et al. 2004), although we have no confirmation of the associated $4.3\mu\text{m}$ CO_2 absorption which is strong in massive protostars.

We have measured the observed fluxes of the fine structure lines in all IRS sources, using the ELF routine in DIPSO, which are presented in Table 4. Other, weaker features are observed in the SH module, including $\text{H}\alpha$ ($\text{H I } 7-6$) at $12.37\mu\text{m}$ ¹, for which $\log[I(\text{H}\alpha)/I([\text{Ne II } 12.8\mu\text{m})] = -1.92 \pm 0.04$. Where appropriate, we include de-reddened line intensities in Table 4, obtained from mean K -band extinctions measured previously together with the mid-IR ex-

¹ At the spectral resolution of IRS/SH the $12.37\mu\text{m}$ feature is actually a blend of $\text{H I } (7-6)$ and $(11-8)$ for which $I(11-8)/I(7-6) = 0.123$ according to Case B recombination theory at $T_e = 7,500\text{ K}$ and 10^4 cm^{-3} (Storey & Hummer 1995).

Table 4. Mid-IR fine structure line fluxes (intensities in bold font), with units of $10^{-14} \text{ W m}^{-2}$, for the O stars and massive YSOs from *Spitzer*/IRS spectroscopy of W31, together with archival *ISO*/SWS observations of selected UC H II regions from Peeters et al. (2002)

Object	A_K	Line Fluxes (Intensities)				$\log \frac{I[\text{NeIII}]}{I[\text{NeII}]}$	$\log \frac{I[\text{SIV}]}{I[\text{SIII}]}$	$\log \frac{I[\text{SIV}]}{I[\text{NeII}]}$
		[SIV] 10.5 μm	[NeII] 12.8 μm	[NeIII] 15.5 μm	[SIII] 18.7 μm			
W31 #1	2.1	0.138 \pm 0.002	9.66 \pm 0.10	1.19 \pm 0.01	11.4 \pm 0.1			
		0.473\pm0.006	12.7\pm0.1	1.46\pm0.02	13.7\pm0.1	-0.94\pm0.01	-0.46\pm0.01	-1.46\pm0.01
W31 #2	2.1	0.452 \pm 0.004	7.43 \pm 0.07	3.96 \pm 0.03	12.7 \pm 0.1			
		1.55\pm0.01	9.78\pm0.1	4.86\pm0.04	15.4\pm0.1	-0.30\pm0.01	-1.00\pm0.01	-0.80\pm0.01
W31 #3	2.1	0.193 \pm 0.002	5.44 \pm 0.05	1.61 \pm 0.02	8.7 \pm 0.1			
		0.66\pm0.01	7.2\pm0.1	2.0\pm0.02	10.5\pm0.1	-0.56\pm0.01	-1.20\pm0.01	-1.03\pm0.01
W31 #4	2.1	0.365 \pm 0.003	7.34 \pm 0.07	3.14 \pm 0.04	11.6 \pm 0.1			
		1.25\pm0.01	9.66\pm0.1	3.85\pm0.05	14.0\pm0.1	-0.40\pm0.01	-1.05\pm0.01	-0.89\pm0.01
W31 #5	2.1	0.010 \pm 0.0001	5.86 \pm 0.7	1.06 \pm 0.01	6.80 \pm 0.1			
		0.341\pm0.003	7.71\pm0.08	1.30\pm0.01	8.2\pm0.1	-0.77\pm0.01	-1.38\pm0.01	-1.35\pm0.01
W31 #9	2.1	0.062 \pm 0.001	7.06 \pm 0.11	0.80 \pm 0.01	8.0 \pm 0.1			
		0.211\pm0.003	9.3\pm0.1	0.99\pm0.01	9.7\pm0.1	-0.97\pm0.01	-1.66\pm0.01	-1.64\pm0.01
W31 #15	2.1	0.301 \pm 0.002	8.04 \pm 0.08	3.02 \pm 0.03	12.8 \pm 0.1			
		1.03\pm0.01	10.6\pm0.1	3.71\pm0.04	15.4\pm0.1	-0.46\pm0.01	-1.18\pm0.01	-1.01\pm0.01
W31 #26	2.1	0.396 \pm 0.004	13.5 \pm 0.1	3.92 \pm 0.03	15.2 \pm 0.2			
		1.36\pm0.01	17.8\pm0.2	4.81\pm0.04	18.3\pm0.2	-0.57\pm0.01	-1.13\pm0.01	-1.12\pm0.01
W31 #30	2.1	0.286 \pm 0.002	12.4 \pm 0.2	3.15 \pm 0.02	14.5 \pm 0.1			
		0.98\pm0.01	16.3\pm0.2	3.87\pm0.03	17.5\pm0.2	-0.63\pm0.01	-1.25\pm0.01	-1.22\pm0.01
G23.96+0.15	2.0	0.33 \pm 0.08	34 \pm 1	2.4 \pm 0.2	25.6 \pm 0.4			
		1.3\pm0.2	46\pm1	3.0\pm0.3	31.7\pm0.5	-1.19\pm0.06	-1.37\pm0.05	-1.54\pm0.05
G29.96-0.02	1.6	4.2 \pm 0.4	99 \pm 7	27 \pm 1	46 \pm 1			
		10.7\pm1	122\pm9	32\pm1	53\pm1	-0.58\pm0.05	-0.69\pm0.05	-1.06\pm0.06

**Figure 7.** Fine structure lines of the O-type stars (filled circles) and massive YSOs (open circles) in W31, with several compact and ultracompact H II regions discussed in this work included for comparison (open triangles). The dashed line is taken from Martín-Hernández et al. (2002b), and represents the best fit to observational datasets spanning a wide range of environments (see text).

tion law of Morris et al. (2000), namely

$$A_{10.5\mu\text{m}} = 0.637 A_K$$

$$A_{12.8\mu\text{m}} = 0.142 A_K$$

$$A_{15.5\mu\text{m}} = 0.106 A_K$$

Of the mid-IR diagnostics, the [S IV] line at 10.51 μm is significantly affected by the 9.7 μm silicate feature. The 11.3 μm PAH emission feature spans a range of equivalent widths, typically $W_\lambda = 600 \pm 300 \text{ \AA}$, with the exception of two massive YSOs, #1 ($W_\lambda \approx 2500 \text{ \AA}$) and #9 ($W_\lambda \approx 2100 \text{ \AA}$). Weak UIR emission at 12.7 μm can be seen in these two sources (see Fig. 6).

In addition to the W31 sources, we also present mid-IR fine structure line fluxes for selected UC H II regions in Table 4. Of these, G23.96+0.15 and G29.96-0.02 lie within the inner Milky Way and possess both mid-IR spectroscopy from Infrared Space Observatory (Peeters et al. 2002) and near-IR spectroscopy of the ionizing star (Hanson et al. 2005; Crowther & Furness 2008). Interstellar extinction for these were taken from Crowther & Furness (2008) and Martín-Hernández et al. (2002a), respectively.

In Fig. 7 we compare the intensity ratios of [NeIII]/[NeII] and [SIV]/[SIII] for the W31 sources plus selected compact and UC H II regions. The former lie close to the best fit of observed ratios in H II regions in the Milky Way and Magellanic Clouds (Martín-Hernández et al. 2002b), based on observations presented by Peeters et al. (2002) and Vermeij et al. (2002). The compact and UC H II regions are apparent outliers, but Fig. 1 from Martín-Hernández et al. (2002b) reveals a typical scatter of 0.2 dex and they did not correct line ratios for interstellar extinction. Physically, these are probably amongst the highest density (ionization parameter) H II regions of the full Martín-Hernández et al. (2002b) sample.

The W31 sources with the highest ionization are the naked O stars #2 (O3-4 V) and #4 (O5.5 \pm 0.5 V) with massive YSOs #1 and #9 possessing the lowest ionization neb-

ulae, with a mixture of naked O stars and massive YSOs at intermediate ionization. From these observations, #15, #26 and #30 could be interpreted as possessing similar stellar properties to #3 ($O5_{-1}^{+0.5}$ V) and #5 ($O5.5 \pm 0.5$ V) with later subtypes for #1 and #9, although we defer a formal estimate of their temperatures until § 4.2. Despite this overlap, it may be significant that the naked O stars tend towards higher ionization nebulae, i.e. higher temperatures (larger stellar masses).

4.2 Photoionization Modelling

The primary aim of our study is to compare the direct near-IR stellar signatures of O stars in W31 (and UC H II regions) with the indirect mid-IR nebular lines through predictions from photoionization models. We use version 08.00 of the photoionization code CLOUDY, last described by Ferland et al. (1998). This solves the equations of thermal and statistical equilibrium for a model nebula, represented by a sphere of gas with uniform density n and filling factor ϵ with a small central cavity which is ionized and heated solely by the UV radiation of a single central star.

Nebular fluxes are predicted, given input abundances, ionizing flux distributions and physical parameters, most important of which is the ionization parameter

$$U = Q_0 / (4\pi R_S^2 n c)$$

and Q_0 is the number of ionizing photons below the H-Lyman edge at 912\AA . Here, R_S is the radius of the Strömgren sphere. Alternatively,

$$U = \frac{1}{c} \left(\frac{n \alpha_B^2 Q_0}{36\pi} \right)^{1/3}$$

where α_B is the Case B recombination coefficient. For a given energy distribution of the ionizing radiation field, any combination of parameters which keeps $Q_H n \epsilon^2$ constant will result in an identical ionization structure of the gas (see Stasińska & Leitherer 1996).

Morisset et al. (2004) have compared a number of stellar atmosphere codes to mid-IR observations of Milky Way H II regions, concluding that the non-LTE codes CMFGEN and WM-Basic (Pauldrach et al. 2001) provide the best match to observations (see also Simón-Díaz & Stasińska 2008). We therefore utilise CMFGEN to provide the ionizing flux distributions, as discussed above.

Ideally, one would employ compact and ultra-compact H II regions that were both spherical and ionized by a single dominant source for such a study. However, such cases are incredibly rare, due to the lack of accurate subtypes for the ionizing stars and scarcity of space borne mid-IR observations. G29.96-0.02 satisfies the ideal criteria relatively well, but G23.96+0.15 is irregular (Wood & Churchwell 1989), and there is ionized gas throughout the W31 cluster. Fortunately, the O stars within W31 are relatively uniform in their ionizing output. In contrast to the ONC, where θ^1 Ori C dominates the extreme UV radiation field, we assume that the ionized gas within IRS apertures centred upon individual O stars are dominated by these stars. In reality, the diffuse radiation field likely reflects a combination of the ionizing photons from multiple cluster members, a consideration which should be borne in mind in the following analysis.

4.2.1 Nebular densities

For the stars whose near-IR spectra enables a spectral type to be determined, we can obtain empirical ionization parameters if the distance and electron density is known. Table 5 provides ionizing parameters for the two UC H II regions whose ionizing stars have been determined from near-IR spectroscopy, G29.96-0.02 and G23.96+0.15, implying $\log U \sim -1.5$ in both cases.

Specifically, for G29.96-0.02, Hanson et al. (2005) estimated $\log Q_0 = 49.6$ for a kinematic distance of 7.4 kpc, which together with a radio-derived Strömgren radius of $3.5''$ (0.13 pc Wood & Churchwell 1989) requires a high electron density of $20,000 \text{ cm}^{-3}$. This is typical of UC H II regions, but is significantly higher than the density of 817 cm^{-3} obtained from ISO observations using $[\text{O III}]$ $88/52\mu\text{m}$ by Martín-Hernández et al. (2002a). For G23.96+0.15, we adopt the kinematic distance of 4.7 kpc for which Crowther & Furness (2008) obtained $\log Q_0 = 49.4$ and we adopt a Strömgren radius of $2''$ (0.025 pc) from Wood & Churchwell (1989), although this UC H II region has an irregular radio morphology. Again, the corresponding electron density of $70,000 \text{ cm}^{-3}$ is much higher than the average density of 1543 cm^{-3} obtained by Martín-Hernández et al. (2002a), arising in part due to the large aperture of ISO/LWS.

It was our intention that the IRS/LH spectroscopy of W31 would have enabled us to deduce electron densities. Unfortunately, due to severe saturation because of the bright dust continuum this was not possible (§ 2.2). We have therefore combined the radio-derived ionizing flux of $\log Q_0 = 50.4$ from Conti & Crowther (2004) with the $30''$ (0.5 pc) radius of the H II region from diffuse Br γ emission (recall Fig. 1) to estimate an electron density of $6,500 \text{ cm}^{-3}$. The ionization parameter implied in all cases is close to $\log U = -1.5$, albeit slightly lower than for the UC H II regions, with similar values anticipated for the massive YSOs in W31. For comparison, Baldwin et al. (1991) also derived $\log U = -1.5$ for the Orion Nebula Cluster (ONC).

4.2.2 Predicted mid-IR fine structure line ratios

Table 5 includes predicted mid-IR fine structure line ratios for each case using CLOUDY. These were obtained with stellar models for individual stars from either Hanson et al. (2005), Crowther & Furness (2008) or the present study and were calculated with abundances scaled to 1.5 times the Solar value, with dust neglected. From a comparison between the observed line ratios in Table 4 and predicted values in Table 5 it is apparent that agreement is very poor. For example, the $[\text{Ne III}]$ $15.5\mu\text{m}/[\text{Ne II}]$ $12.8\mu\text{m}$ and $[\text{S IV}]$ $10.5\mu\text{m}/[\text{S III}]$ $18.7\mu\text{m}$ ratios differs by 1.5 ± 0.5 dex in all cases. This suggests either that the stellar or photoionization models are at fault, or the problem arises from local background variations close to individual W31 sources. The former would appear to be more plausible, since the latter explanation would not reconcile differences between ISO observations of UC H II regions and predictions.

Regardless of the origin for the discrepancy, we have calculated a grid of photoionization models for three ionization parameters, $\log U = -1, -2$ and -3 using stellar atmospheric models appropriate for solar metallicity O dwarfs,

Table 5. Predicted mid-IR fine structure line ratios for inner Milky Way H II regions. Elemental abundances are scaled to $1.5 Z_{\odot}$ throughout. An electron density of $6,500 \text{ cm}^{-3}$ is used for W31 on the basis of the radio-derived ionizing flux ($10^{50.4} \text{ ph s}^{-1}$) and radius of $\sim 30''$ (0.5 pc at a distance of 3.3 kpc) for the giant H II region.

Star	Sp. Type	T_{eff} kK	d kpc	$\log Q_0$	n_e cm^{-3}	R_s pc	$\log U$	$\log \frac{I[\text{NeIII}]}{I[\text{NeII}]}$	$\log \frac{I[\text{SIV}]}{I[\text{SIII}]}$	$\log \frac{I[\text{ArIII}]}{I[\text{NeII}]}$	$\log \frac{I[\text{SIV}]}{I[\text{NeII}]}$	$\log \frac{I[\text{Br}\alpha]}{I[\text{NeII}]}$
W31 #2	O3–4 V	45	3.3	49.6	6,500	(0.24)	–1.6	1.01	0.42	0.52	1.22	–0.01
W31 #3	O5 $^{+0.5}_{-1}$ V	43	3.3	49.3	6,500	(0.19)	–1.7	0.65	0.23	0.28	0.81	–0.28
W31 #4	O5.5 \pm 0.5 V	41	3.3	49.0	6,500	(0.15)	–1.8	0.24	0.01	0.05	0.39	–0.52
W31 #5	O5.5 \pm 0.5 V	41	3.3	49.3	6,500	(0.19)	–1.7	0.31	0.09	0.08	0.49	–0.48
G29.96–0.02	O4–5 V	41	7.4	49.6	20,000	0.13	–1.5	0.95	0.60	0.49	1.06	0.00
G23.96+0.15	O7.5 V	38	4.7	49.2	70,000	0.05	–1.4	0.02	0.46	–0.06	0.02	–0.52

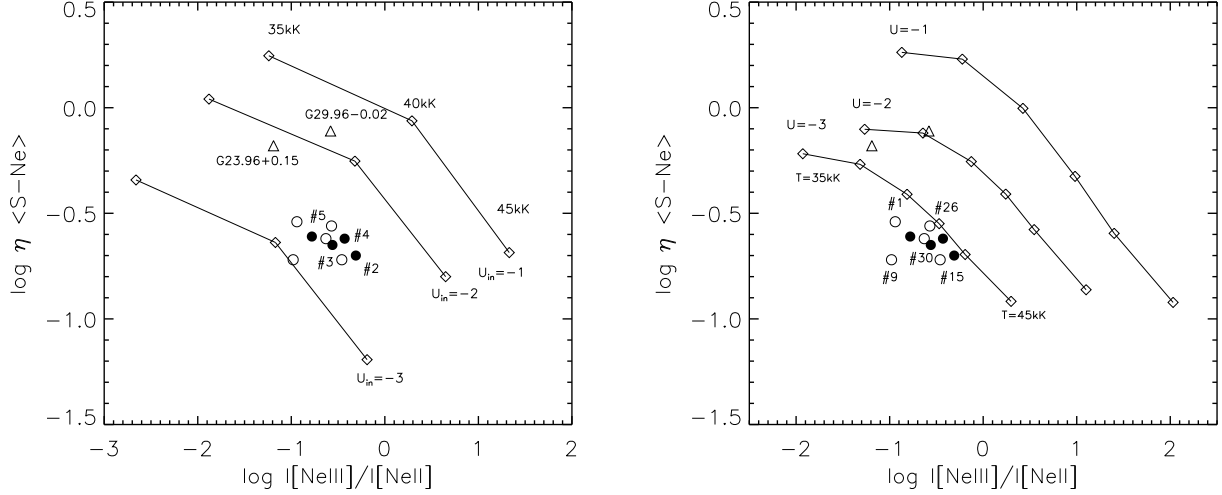


Figure 8. $\log \eta(\text{S-Ne})$ versus $\log [\text{NeIII}]/[\text{NeII}]$ for solar metallicity models from Simón-Díaz & Stasińska (2008) (left panel, $\log U_{\text{in}} = -1, -2, -3$) and this work (right panel, $\log U = -1, -2, -3$), together with empirical data for naked O stars (filled circles, identified in left panel) and massive YSOs (open circles, identified in right panel) in W31, plus UC H II regions (triangles, identified in left panel). See text for a discussion of the key differences between these photoionization models.

as listed in Table 6. These were obtained from the O star calibration from Conti et al. (2008) together with the Vink, de Koter & Lamers (2001) mass-loss prescription. A uniform rotational broadening of 200 km s^{-1} was applied to synthetic spectra. Dust was not included, but has little effect upon the predicted line intensities with Orion-like dust grain compositions for dust-to-gas mass ratios of 0.1–2%. In the unlikely case of Milky Way ISM dust grains with a dust-to-gas mass ratio of 2%, line intensity ratios may be affected by up to factor of two.

Observed line intensities are intrinsically linked to both ionization parameter, U , and stellar temperature, T_{eff} . One means of isolating the form of the radiation field is through the ionization softness parameter $\eta = ([\text{O II}]/[\text{O III}])/([\text{S II}]/[\text{S III}])$ defined for H II regions detected optically by Vílchez & Pagel (1988). Analogously, the hardness of mid-IR nebular diagnostics can be characterised by

$$\eta(\text{S-Ne}) = \frac{([\text{S IV}]10.5\mu\text{m}/[\text{S III}]18.7\mu\text{m})}{([\text{Ne III}]15.5\mu\text{m}/[\text{Ne II}]12.8\mu\text{m})}$$

as discussed by Morisset (2004). Variations in U and T_{eff} are broadly independent in a plot of $\eta(\text{S-Ne})$ versus

$[\text{Ne III}]/[\text{Ne II}]$. In Fig. 8 we compare our CLOUDY predictions for Solar composition nebulae for $\log U = -1, -2, -3$ to the observed positions of W31 stars and UC H II regions, together with recent predictions from Simón-Díaz & Stasińska (2008) which are also based on CLOUDY and CMFGEN models. The W31 sources lie very close together in Fig. 8, with the marginal exception of the massive YSO #9. This source is also an outlier in Fig. 7, possibly as a result of a reduced density (ionization parameter).

G29.96–0.02 lies close to the $(T_{\text{eff}}, \log U_{\text{in}}) = (40\text{kK}, -2)$ photoionization model from Simón-Díaz & Stasińska (2008), in reasonable agreement with the empirical properties of (41kK, –1.5) from Table 5. In contrast, our results predict rather poor agreement for G29.96–0.02 since it sits close to the (37kK, –2) photoionization model. The reason for this difference is that Simón-Díaz & Stasińska (2008) adopt a non-standard model dependent definition of ionization parameter, namely

$$U_{\text{in}} = Q_0/(4\pi R_{\text{in}}^2 n_c)$$

which is based upon the *inner* radius of the model cloud, R_{in} for the photoionization calculation rather than the

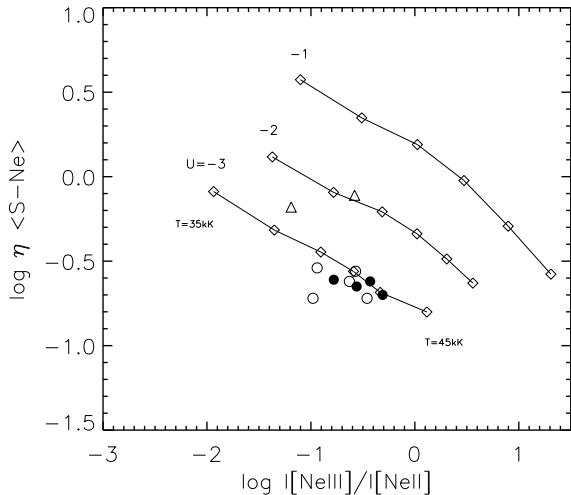


Figure 9. $\log \eta(\text{S-Ne})$ versus $\log I[\text{NeIII}]/I[\text{NeII}]$ ratio for $2\times$ Solar metallicity grid for $\log U = -1, -2, -3$. Symbols have the same meaning as in Fig. 8.

Strömgren radius, R_S . Consequently, the poor agreement for G29.96–0.02 obtained here simply confirms the previous (poor) consistency discussed by Morisset et al. (2002) and Martín-Hernández et al. (2002b). The comparison for G23.96+0.15 fares little better, with $(T_{\text{eff}}, \log U) = (36\text{kK}, -2)$ predicted, in contrast to empirical estimates of $(38\text{kK}, -1.4)$ from Table 5. The situation for the W31 O stars is fairly similar, with ionization parameters of $\log U < -3$ predicted in the right panel of Fig. 8, yet -1.7 is more typical of compact and UC H II regions (Table 5).

In § 3.2, we indicated that W31 is anticipated to be metal-rich with respect to the Solar neighbourhood. Similar arguments apply for G23.96+0.15 and especially G29.96–0.02. For a kinematic distance of ~ 7 kpc to G29.96–0.02, this UC H II region would lie at $R_{\text{GC}} = 4$ kpc from the Galactic Centre², versus 3.7 kpc for G23.96+0.15 for a kinematic distance of 4.7 kpc.

Therefore, we have also calculated a set of super-solar ($2 Z_{\odot}$) CLOUDY models, based upon O star models that are identical to the solar composition grid except that both metal abundances and mass-loss rates are increased (see Table 6 for the latter). Solely early O stars provide significant numbers of extreme UV photons capable of producing [NeIII] and [SIV] nebular emission while [NeII] and [SIII] emission is expected to cease beyond $\sim \text{O9.5V}$.

Predictions from $2Z_{\odot}$ photoionization models are presented in Fig. 9. In general, from a comparison with the Solar models, these yield slightly higher stellar temperatures and ionization parameters. G29.96–0.02 lies close to $(T_{\text{eff}}, \log U) = (38\text{kK}, -2)$, representing a slight improvement with respect to the empirical temperature. Similar comments apply for G23.96+0.15, although predicted temperatures remain too low, and ionization parameters are offset by -1.0 to -1.5 dex for G23.96+0.15 and the O stars in W31.

² Sewilo et al. (2004) obtained a distance of 8.9 kpc or $R_{\text{GC}} = 4.5$ kpc to G29.96–0.02.

Table 6. Stellar parameters for solar (twice solar) O dwarf model atmospheres used in photoionization calculations, based upon calibrations presented in Conti et al. (2008) with mass-loss rates obtained from the Vink et al. (2001) prescriptions.

Subtype	T_{eff} kK	$\log L$ L_{\odot}	M M_{\odot}	$\log Q_0$	v_{∞} km s^{-1}	$\log \dot{M}$ $M_{\odot} \text{ yr}^{-1}$
O3 V	45	5.88	74	49.65	3200	−5.41 (−5.15)
O4 V	43	5.77	64	49.5	3000	−5.55 (−5.30)
O5 V	41	5.57	51	49.25	2900	−5.86 (−5.61)
O6 V	39	5.39	41	49.0	2600	−6.12 (−5.86)
O7 V	37	5.25	36	48.8	2300	−6.33 (−6.07)
O8 V	35	5.10	31	48.55	1750	−6.49 (−6.23)
O9 V	33	4.91	25	48.2	1500	−6.79 (−6.53)
O9.5 V	31.5	4.78	23	48.0	1200	−6.97 (−6.72)

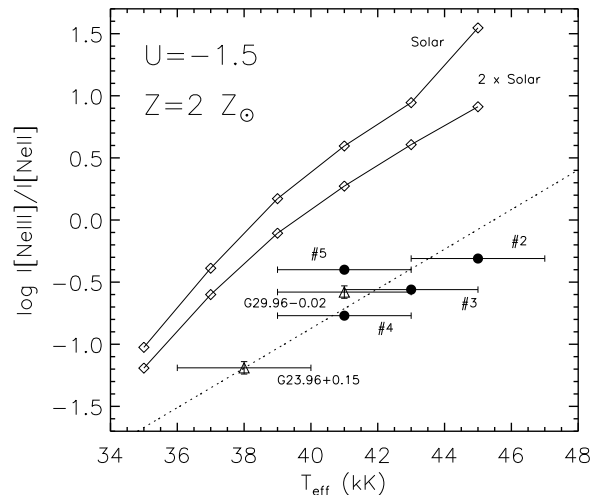


Figure 10. Comparison between the predicted [NeIII]/[NeII] intensity ratio and effective temperature for $\log U = -1.5$ models at Solar and $2\times$ Solar composition. Empirical data are naked O stars in W31 (filled circles) and inner Milky Way UC H II regions (open triangles) together with a first order fit to the empirical datasets (dotted line, see text).

4.3 [NeIII]/[NeII] calibrations

Let us now focus upon the predicted [NeIII]/[NeII] ratio versus stellar temperature, which is presented in Fig 10 for the Solar and $2\times Z_{\odot}$ metallicity grids at $\log U = -1.5$. We have selected this value for the ionization parameter since this is characteristic of compact and especially UC H II regions in our sample. Empirical results are also shown, with stellar temperatures drawn from Table 5, quantifying earlier discrepancies with respect to the predictions. An explanation for the disagreement is not readily apparent, although it may involve incomplete line blanketing in current non-plane parallel model atmospheres at high energies. Nevertheless, observations allow us to estimate the temperatures of the ionizing O stars in other dense H II regions (for which $\log U \sim -1.5$) within the inner Milky Way, to within $\pm 2\text{kK}$ (i.e. one spectral subtype) in principle. A first order fit to

Table 7. Estimates of spectral types of the ionizing stars responsible for compact and ultra-compact H II regions in the inner Milky Way ($R_{GC} < 7$ kpc) from Peeters et al. (2002) plus massive YSOs in W31 from the present study. Interstellar extinctions are taken from the present study, Martín-Hernández et al. (2002a), or $A_K = 1.6$ mag otherwise (marked with *). Kinematic distances adopt a Solar galactocentric distance of 8.0 kpc (Reid 1993). Temperatures and spectral types are obtained for both the [Ne III]/[Ne II] and [S IV]/[Ne II] diagnostic ratios.

Source	IRAS	Alias	V_{LSR} km s ⁻¹	d kpc	R_{GC} kpc	Ref	A_K mag	$\log \frac{[Ne III]}{[Ne II]}$	T_{eff} kK	Sp Type	$\log \frac{[S IV]}{[Ne II]}$	T_{eff} kK	Sp Type
G1.13-0.11	17455-2800	Sgr D	-17.1	8.0	0.2	a	1.8	-0.36	43	O4 V	-0.69	43	O4 V
W31 #1				3.3	4.8	k	2.1	-0.94	39.5	O6 V	-1.46	39	O6 V
W31 #9				3.3	4.8	k	2.1	-0.97	39.5	O6 V	-1.64	38	O6.5 V
W31 #15				3.3	4.8	k	2.1	-0.46	42.5	O4 V	-1.01	41.5	O5 V
W31 #26				3.3	4.8	k	2.1	-0.57	42	O4-5 V	-1.12	41	O5 V
W31 #30				3.3	4.8	k	2.1	-0.63	41.5	O5 V	-1.22	40	O5.5 V
G33.91+0.11	18502+0051		-100.0	6.6	4.5	b, c	1.6*	-0.66	42	O4-5 V	-1.18	41	O5 V
G49.20-0.35	19207+1410		-67.9	5.2	6.1	d	1.6*	+0.03	45	O3 V	-0.23	45	O3 V
G301.11+0.97	12331-6134		-40.8	4.1	6.8	h	1.6*	-0.16	44	O3-4 V	-0.38	44	O3-4 V
G326.44+0.91	15384-5348		-41.0	2.5	6.1	h	1.3	-0.55	42	O4-5 V	-0.86	42	O4-5 V
G328.31+0.43	15502-5302		-91.7	5.4	4.4	h	2.7	-0.63	42	O4-5 V	-1.18	41	O5 V
G332.15-0.45	16128-5109		-55.7	3.5	5.2	h	1.6*	-0.26	43.5	O4 V	-0.66	43	O4 V
G351.46-0.44	17221-3619		-22.3	3.3	4.8	h	1.8	-1.41	39	O6 V	-1.54	40	O5.5 V

(a) Mehringer et al. (1998); (b) Wood & Churchwell (1989); (c) Fish et al. (2003); (d) Sewilo et al. (2004); (e) Araya et al. (2002); (f) Maciel & Dutra (1992); (g) Quireza et al. (2006); (h) Bronfman, Nyman & May (1996); (i) Afflerbach et al. (1996); (j) Caswell & Haynes (1987); (k) this study

the empirical datasets using IDL’s polyfit routine reveals

$$(T_{eff}/kK)_{2Z_{\odot}} = +45.47 \pm 1.37 \\ +6.27 \pm 1.96(\log I[Ne III]/I[Ne II]).$$

O subtypes may then be estimated from the recent T_{eff} calibration of Martins, Schaerer & Hillier (2005). Of course, this approach is only practical for compact and UC H II regions ionized by early- and mid- O stars, in view of the weakness of [Ne III] 15.5 μ m for late O-types.

To illustrate its potential diagnostic role, in Table 7 we provide stellar temperatures derived from extinction corrected [Ne III]/[Ne II] ratios for compact and ultra-compact H II regions from ISO/SWS observations (Peeters et al. 2002), plus the massive YSO’s in W31 from the present study. Extinctions are either taken from Martín-Hernández et al. (2002a), or $A_K = 1.6$ mag is adopted otherwise. We omit the peculiar compact H II region G93.53+1.47 (M1-78) from this sample (Martín-Hernández et al. 2008). For the massive YSO’s in W31, Table 7 presents spectral types inferred from the mean interstellar extinction obtained from the naked W31 O stars. In reality, higher extinctions may be expected for these cases (recall § 3.3). Fortunately, the use of a higher extinction does not affect the resulting stellar temperatures/subtypes. For #26, a subtype of O4-5V is obtained, versus an approximate subtype of O6V from its H-band ISAAC spectrum (§ 3.3).

Since our calibration has been established using solely compact H II regions within the inner Milky Way - with super-solar elemental abundances - one should consider separately the case of H II regions close to, or exterior to, the Solar circle. Of course, metal content is very relevant to gas cooling and metal-line blanketing of the extreme UV energy distributions of O stars. Unfortunately, among the compact H II regions close to the Solar circle, very few possess both mid-IR spectroscopy and well determined properties for the dominant ionizing star. The ONC - for which θ^1 Ori C (HD

37022, O6-7 Vp) is the dominant source of ionizing radiation - is one such case in that it possesses both mid-infrared spectroscopy Simpson et al. (1998) and a contemporary analysis of its stellar content by Simón-Díaz et al. (2006).

Other examples are generally complicated by the presence of multiple ionizing stars of uncertain spectral type (e.g. NGC 7538) or mid-IR spectroscopy is lacking. The only other case for which mid-IR spectroscopy is available together with a well determined spectral type of the ionizing star is G110.10+0.05 (IC 1470, Sh 2-156) for which Hunter & Massey (1990) derived O6.5 V for its ionizing star. Therefore, we refrain from attempting a solar metallicity calibration at this time. However, we are able to compare the ONC with the CLOUDY predictions, recalling that Baldwin et al. (1991) derived a value of $\log U = -1.48$ for the ONC. In contrast to the metal-rich H II regions, the observed neon ratio for the ONC is in better agreement with the solar-metallicity predictions for $T_{eff} = 39 \pm 1$ kK for θ^1 Ori C (Simón-Díaz et al. 2006).

4.4 [S IV]/[Ne II] and [Ar III]/[Ne II] calibrations

Of course, neither η (S-Ne) nor [Ne III]/[Ne II] are available from ground-based observations. In such cases, only [Ar III] 8.9 μ m, [S IV] 10.5 μ m and [Ne II] 12.8 μ m are accessible. In Figure 11 we compare the [S IV]/[Ne II] ratio versus stellar temperature for sources in W31, G29.96-0.02 and G23.96+0.15, plus CLOUDY predictions for 2 \times Solar stellar models.

The comparison between the predicted [S IV]/[Ne II] ratio and empirical results is much poorer than for the [Ne III]/[Ne II] ratio. As such, one might conclude that no straightforward means of determining temperatures exists from ground-based data alone. However, it has been established that there is a reasonably tight correlation between the [S IV]/[Ne II] and [Ne III]/[Ne II] ratios, as shown

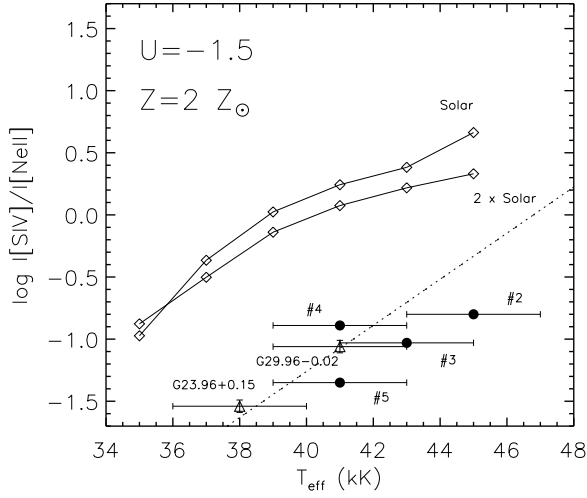


Figure 11. Effective temperature versus $\log [\text{SIV}]/[\text{NeII}]$ for our $\log U = -1.5$ solar and $2\times$ Solar models together with inner Milky Way sources and resulting empirical calibration (dotted-line).

by Groves, Neff & Brandl (2008). For the sample of Milky Way compact H II regions observed by Peeters et al. (2002) we obtain a linear, least-squares fit

$$\log I[\text{NeIII}]/I[\text{NeII}] = 0.86 \pm 0.06(\log I[\text{SIV}]/I[\text{NeII}]) + 0.21 \pm 0.06$$

after correcting line fluxes for extinction (as discussed above). This is presented in Fig. 12. For comparison, Groves et al. (2008) obtained coefficients 0.74 and 0.42 for 65 Galactic H II regions from Giveon et al. (2002), *neglecting* interstellar extinction.

We use this conversion to apply our empirical $[\text{NeIII}]/[\text{NeII}]$ temperature calibration to $[\text{SIV}]/[\text{NeII}]$. This is also presented in Fig. 11, from which similar consistency with empirical results to that achieved for $[\text{NeIII}]/[\text{NeII}]$ is obtained, revealing

$$(T_{\text{eff}}/kK)_{2Z_{\odot}} = +46.79 \pm 1.51 + 5.39 \pm 1.69(\log I[\text{SIV}]/I[\text{NeII}])$$

for the super-solar case. Again, we include the predicted subtypes of Galactic compact H II regions from our empirical $[\text{SIV}]/[\text{NeII}]$ calibrations in Table 7. Since $[\text{SIV}]$ is relatively sensitive to extinction, if we were to use extinctions inferred from their H-K colours (e.g. $A_K = 4.9$ mag for W31 #26) rather than the average of the naked O stars, we would obtain temperatures up to 3kK higher. It is likely that their actual extinctions lie between these two extremes due to the contribution of hot circumstellar dust.

In principle, either the $[\text{NeIII}]/[\text{NeII}]$ or $[\text{SIV}]/[\text{NeII}]$ calibration may be applied to H II regions ionized by early or mid-type O stars, since late-type O stars possess too low photon fluxes at the energies required to produce either Ne^{2+} ($\geq 41\text{eV}$) or S^{3+} ($\geq 35\text{eV}$). Therefore, we have also considered the potential role of $[\text{ArIII}]$ 9.0 μm from the two UC H II regions (this line was not covered by IRS/SH datasets). For the Peeters et al. (2002) sample of H II regions as discussed above, we obtained $[\text{ArIII}]$ line intensities using

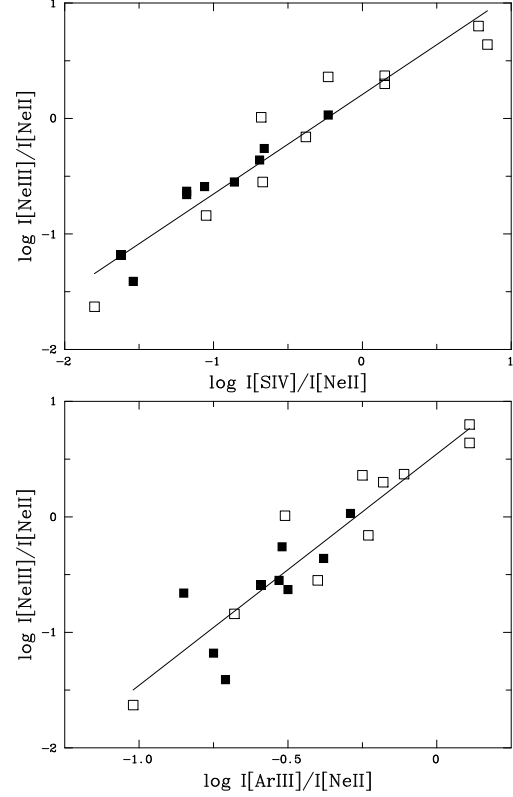


Figure 12. (Upper panel) Correlation between $I[\text{SIV}]/I[\text{NeII}]$ and $I[\text{NeIII}]/I[\text{NeII}]$ for H II regions located in the inner (filled squares) and outer (open squares) Milky Way using ISO/SWS fluxes from Peeters et al. (2002), dereddened as described in the text; (lower panel) As above except for correlation between $I[\text{ArIII}]/I[\text{NeII}]$ and $I[\text{NeIII}]/I[\text{NeII}]$.

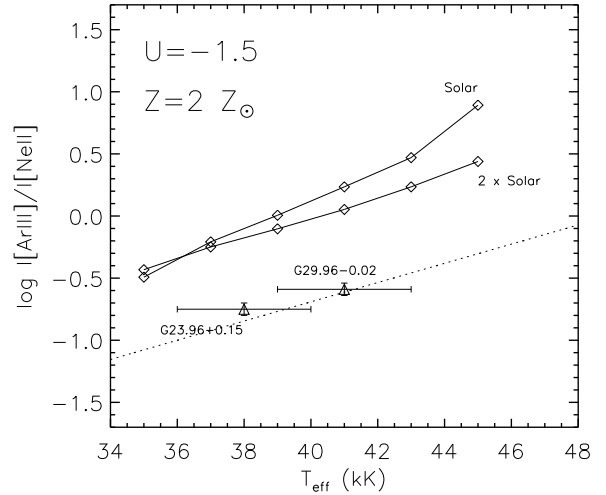


Figure 13. Effective temperature versus $\log [\text{ArIII}]/[\text{NeIV}]$ for our $\log U = -1.5$ solar and $2\times$ Solar models together with inner Milky Way sources and resulting empirical calibration (dotted-line).

an extinction correction of

$$A_{9.0\mu\text{m}} = 0.719 A_K$$

and obtained a similar quality fit to that of $I[\text{S IV}]/I[\text{Ne II}]$ above (see Fig. 12), namely

$$\log I[\text{Ne III}]/I[\text{Ne II}] = 2.06 \pm 0.21(\log I[\text{Ar III}]/I[\text{Ne II}]) + 0.55 \pm 0.11$$

allowing estimates of temperatures to be made from the $[\text{Ar III}]/[\text{Ne II}]$ ratio. Unfortunately, this is relatively insensitive to temperature and so should only be considered if *neither* of the primary calibrations are available. Nevertheless, the comparison between empirical results for G23.96+0.15 and G29.96–0.02 and our metal-rich calibration, presented in Fig. 13, is reasonable. For completeness, the super-solar calibration may be expressed as:

$$(T_{\text{eff}}/kK)_{2Z_{\odot}} = +48.92 \pm 1.79 + 12.92 \pm 3.47(\log I[\text{Ar III}]/I[\text{Ne II}])$$

It should be re-emphasised that these calibrations are solely intended for compact and ultra-compact H II regions for the inner Milky Way, and are liable to revision once additional empirical results become available. Nevertheless, it is apparent that the use of any mid-IR nebular diagnostics to establish properties of metal-rich O stars will lead to stellar temperatures that are too low, by as much as 5 kK or 10%.

5 DISCUSSION

5.1 Massive Star Content of W31

Let us now return to W31 itself, and specifically its massive star content. From Fig. 7, the highest ionization stars are naked O stars including the highest mass star in W31 #2, while the lowest ionization stars (#1, #9) are massive YSOs with presumably the lowest masses.

Ideally, one would like to comment upon differences in timescales over which circumstellar material is destroyed by young O stars of different masses, but the range of masses exhibited by our sample is likely to be relatively modest (with the exception of #2) and the unusual geometry of W31 suggests that massive star formation across this cluster was not necessarily coeval. The only naked O star from Fig. 4 suggesting an age spread is #5. However, as discussed in § 3.2 it is plausible that #5 is a close binary with similar mass components from which a uniform cluster age would be obtained.

For the case of a genuinely coeval cluster, it is likely that stars with the highest luminosities – and hardest extreme UV photon fluxes – destroy circumstellar dust more rapidly than lower luminosity, softer extreme UV stars, which are conceivably the massive YSOs. From Table 7 stellar subtypes of O4–6V are obtained from our $[\text{Ne III}]/[\text{Ne II}]$ calibration (Table 7), i.e. comparable to the naked O stars.

W31 #26, in particular, appears to be in the process of actively clearing its circumstellar dust, revealing photospheric absorption lines, consistent with a subtype of O6V, slightly later than the indirect calibration. #15 and #30, on the basis of similar neon ratios to #26 its mid-IR neon lines likely possess similar subtypes, with ~O6–6.5 subtypes for

#1 and #9. The lowest (current) mass estimated amongst the naked O stars is $\sim 36M_{\odot}$ for the O5.5V star #4 (Table 3). Consequently, it is likely that the massive YSO's possess stellar masses of order 30–35 M_{\odot} . Recall also that W31 also hosts a number of UC H II regions (Ghosh et al. 1989). Such sources are still too deeply embedded to be detected at near-IR wavelengths, most likely as a result of still lower luminosities/masses (late O subtypes?). If the UC H II regions are genuinely coeval with the naked O stars and massive YSO's in W31, a timescale in excess of 0.5 Myr is required for late O stars to sufficiently clear their environment to be detected at near-IR wavelengths.

5.2 Analysis of embedded stellar populations from mid-IR fine structure lines.

Our study has focused upon compact and ultra-compact H II regions within the inner Milky Way. We find that all mid-IR nebular diagnostics will lead to stellar temperatures that are too low, by as much as 5 kK or 10%. However, mid-IR fine structure lines also have application in external galaxies, ranging from metal-rich H II regions in spiral galaxies (Rubin et al. 2007), starbursts (Thornley et al. 2000; Verma et al. 2003; Brandl et al. 2006) and ultraluminous infrared galaxies (ULIRGs Lutz et al. 1998).

Within this diverse sample, the mid-IR has the greatest diagnostic role for the highly obscured cases, either young, embedded massive clusters within metal-poor starbursts such as NGC 5253 (Crowther et al. 1999), He 2–10 (Vacca et al. 2002), or metal-rich ULIRG's (Genzel et al. 1998).

Of course, the aim of studies of starbursts is generally to obtain ages and/or stellar content (mass, Initial Mass Function) yet similar approaches to the present study are usually followed, involving photoionization models and ionizing flux distributions from stellar atmosphere models coupled to evolutionary predictions through population synthesis codes (e.g. Pindao et al. 2002).

Problems highlighted here and elsewhere (Morisset et al. 2002; Martín-Hernández et al. 2002a,b) for H II regions in the *inner* Milky Way probably have their origins in both (i) incomplete opacities from all relevant ions in stellar atmosphere models allowing for non-LTE effects and stellar winds; (ii) 1D photoionization models. In principle, the second of these can be tested against 3D photoionization codes such as MOCASSIN (Ercolano, Barlow & Storey 2005). Until then, similar empirical calibrations of photoionization models across a range of metallicities may be the best approach. It may be significant that the discrepancy for the Orion Nebula Cluster is significantly less severe than for G29.96–0.02 and G23.96+0.15. A further test would be for an extensive sample of H II regions in the outer Milky Way and the Magellanic Cloud. These could potentially include 30 Doradus (LMC) and/or NGC 346 (SMC). Beyond the Magellanic Clouds, spatial resolution prevents spectroscopy of individual stars within compact star clusters.

6 SUMMARY

We present near-IR (VLT/ISAAC) and mid-IR (*Spitzer*/IRS) spectroscopy of massive stars within the young Milky Way cluster G10.2–0.3 (W31). Our main results may be summarised as follows:

(i) *H*- and *K*-band spectroscopy of naked O stars broadly confirms subtypes from Blum et al. (2001) from which a refined cluster distance (3.3 kpc) and age (~ 0.6 Myr) are obtained.

(ii) W31 #26, one of the massive YSOs from Blum et al. (2001) is shown to possess photospheric features, consistent with a subtype of O6V, in addition to near-IR circumstellar dust emission. This suggests it is in the very process of clearing its immediate environment.

(iii) Mid-IR fine-structure line ratios of W31 stars overlap with other Milky Way and Magellanic Cloud H II regions on a [Ne III]/[Ne II] to [S IV]/[S III] diagram.

(iv) Following Morisset et al. (2004), a comparison of the mid-IR radiation hardness parameter, $\eta(\text{S-Ne}) = ([\text{Ne III}]/[\text{Ne II}])/([\text{S IV}]/[\text{S III}])$ versus [Ne III]/[Ne II] allows dependencies upon effective temperature and ionization parameter, U to be tested. Predicted solar metallicity (stellar and nebular) models differ greatly from empirical T_{eff} and U , with small improvements in both for $2\times$ solar grids.

(v) Similar studies are planned for metal-poor environments, which should establish whether the problem is most severe at high metallicity. Initial results for the ONC do show an improved agreement between predictions and observations, although larger samples are required for statistically robust results. If the discrepancy were to disappear at lower metallicities it would suggest that either the extreme UV metal line blanketing of early-types stars is incomplete, or there is a problem with photoionization models at high metallicity.

(vi) We show that an empirical correction to the predicted [Ne III]/[Ne II] ratio against T_{eff} for $\log U = -1.5$ and $2\times Z_{\odot}$ provides a reasonable match to stellar results for W31 and two inner Milky Way UC H II regions. Estimates of the O subtypes of the ionizing stars in other inner Galactic H II regions ($R_{\text{GC}} < 7$ kpc) are obtained. This approach is only practical for early- and mid- O stars, in view of the weakness of [Ne III] $15.5\mu\text{m}$ for late O-types.

(vii) For ground-based datasets lacking [Ne III] observations, we have used a correlation between [Ne III]/[Ne II] and [S IV]/[Ne II] – see also Groves et al. (2008) – to provide a calibration of [S IV]/[Ne II] against T_{eff} for super-solar compact H II regions. Since only early- and mid- O stars provide significant [S IV] emission, we have also obtained a similar relation for $9.0\mu\text{m}$ [Ar III]/ $12.8\mu\text{m}$ [Ne II] versus T_{eff} , although this should only be applied when other diagnostics are unavailable, with both [Ar III] and [Ne II] expected to be weak in late-type O stars.

Finally, in view of the apparent discrepancy between stellar and nebular results at high metallicity compact H II regions, studies of more straightforward templates are sought, to enable the present calibration to be put on a more robust footing.

ACKNOWLEDGEMENTS

JPJ would like to acknowledge financial support from STFC, CLB acknowledges financial support from FAPESP and PSC thanks the NSF for continuous support. We wish to thank John Hillier and Gary Ferland for maintaining CMFGEN and CLOUDY. Specific support for this work was partly provided by NASA through an award issued by JPL/Caltech. We appreciate many useful suggestions from an anonymous referee.

REFERENCES

- Afflerbach A., Churchwell E., Acord J. M., Hofner P., Kurtz S., Depree C. G., 1996, *ApJS*, 106, 423
- Allison R. J., Goodwin S. P., Parker R. J., Portegies Zwart S. F., de Grijs R., Kouwenhoven M. B. N., 2009, *MNRAS*, 395, 1449
- Araya E., Hofner P., Churchwell E., Kurtz S., 2002, *ApJS*, 138, 63
- Asplund M., Grevesse N., Sauval A. J., Allende Prieto C., Kiselman D., 2004, *A&A*, 417, 751
- Baldwin J. A., Ferland G. J., Martin P. G., Corbin M. R., Cota S. A., Peterson B. M., Slettebak A., 1991, *ApJ*, 374, 580
- Barbosa C. L., Blum R. D., Conti P. S., Daminieli A., Figueredo E., 2008, *ApJ*, 678, L55
- Blum R. D., Daminieli A., Conti P. S., 2001, *AJ*, 121, 3149
- Blum R. D., McGregor P. J., 2008, *AJ*, 135, 1708
- Blum R. D., McGregor P. J., 2009, *AJ*, 138, 489
- Brandl B. R., Bernard-Salas J., Spoon H. W. W., et al. 2006, *ApJ*, 653, 1129
- Bronfman L., Nyman L.-A., May J., 1996, *A&AS*, 115, 81
- Caswell J. L., Haynes R. F., 1987, *A&A*, 171, 261
- Churchwell E., 2002, *ARA&A*, 40, 27
- Clarke C. J., Bonnell I. A., 2008, *MNRAS*, 388, 1171
- Conti P. S., Crowther P. A., 2004, *MNRAS*, 355, 899
- Conti P. S., Crowther P. A., Leitherer C., 2008, *From Luminous Hot Stars to Starburst Galaxies*. Cambridge Astrophysics Series Vol. 45, Cambridge University Press
- Cox A. N., 2000, *Allen's Astrophysical Quantities*, 4th ed.. Springer
- Crowther P. A., Beck S. C., Willis A. J., Conti P. S., Morris P. W., Sutherland R. S., 1999, *MNRAS*, 304, 654
- Crowther P. A., Furness J. P., 2008, *A&A*, 492, 111
- de Grijs R., Gilmore G. F., Johnson R. A., Mackey A. D., 2002, *MNRAS*, 331, 245
- Ercolano B., Barlow M. J., Storey P. J., 2005, *MNRAS*, 362, 1038
- Esteban C., García-Rojas J., Peimbert M., Peimbert A., Ruiz M. T., Rodríguez M., Carigi L., 2005, *ApJ*, 618, L95
- Fazio G. G., Hora J. L., Allen L. E., et al. 2004, *ApJS*, 154, 10
- Ferland G. J., Korista K. T., Verner D. A., Ferguson J. W., Kingdon J. B., Verner E. M., 1998, *PASP*, 110, 761
- Fish V. L., Reid M. J., Wilner D. J., Churchwell E., 2003, *ApJ*, 587, 701
- Genzel R., Lutz D., Sturm E., et al. 1998, *ApJ*, 498, 579
- Ghosh S. K., Iyengar K. V. K., Rengarajan T. N., Tandon S. N., Verma R. P., Daniel R. R., 1989, *ApJ*, 347, 338
- Gibb E. L., Whittet D. C. B., Boogert A. C. A., Tielens A. G. G. M., 2004, *ApJS*, 151, 35

- Giveon U., Sternberg A., Lutz D., Feuchtgruber H., Pauldrach A. W. A., 2002, *ApJ*, 566, 880
- Groves B., Nefs B., Brandl B., 2008, *MNRAS*, 391, L113
- Hanson M. M., Kudritzki R.-P., Kenworthy M. A., Puls J., Tokunaga A. T., 2005, *ApJS*, 161, 154
- Hanson M. M., Luhman K. L., Rieke G. H., 2002, *ApJS*, 138, 35
- Hanson M. M., Puls J., Repolust T., 2005, in Cesaroni R., Felli M., Churchwell E., Walmsley M., eds, *IAU Symposium* 227, p. 376
- Hillier D. J., Lanz T., Heap S. R., Hubeny I., Smith L. J., Evans C. J., Lennon D. J., Bouret J. C., 2003, *ApJ*, 588, 1039
- Hillier D. J., Miller D. L., 1998, *ApJ*, 496, 407
- Houck J. R., Roellig T. L., van Cleve J., et al. 2004, *ApJS*, 154, 18
- Hunter D. A., Massey P., 1990, *AJ*, 99, 846
- Indebetouw R., Mathis J. S., Babler B. L., Meade M. R., Watson C., Whitney B. A., Wolff M. J., Wolfire M. G., 2005, *ApJ*, 619, 931
- Kessler M. F., Steinz J. A., Anderegg M. E., et al. 1996, *A&A*, 315, L27
- Kurtz S., Churchwell E., Wood D. O. S., 1994, *ApJS*, 91, 659
- Lanz T., Hubeny I., 2003, *ApJS*, 146, 417
- Lejeune T., Schaerer D., 2001, *A&A*, 366, 538
- Lumsden S. L., Puxley P. J., Hoare M. G., Moore T. J. T., Ridge N. A., 2003, *MNRAS*, 340, 799
- Lutz D., Genzel R., Sternberg A., et al. 1996, *A&A*, 315, L137
- Lutz D., Spoon H. W. W., Rigopoulou D., Moorwood A. F. M., Genzel R., 1998, *ApJ*, 505, L103
- Maciel W. J., Dutra C. M., 1992, *A&A*, 262, 271
- Martín-Hernández N. L., Esteban C., Mesa-Delgado A., Bik A., Puga E., 2008, *A&A*, 482, 215
- Martín-Hernández N. L., Peeters E., Morisset C., Tielens A. G. G. M., Cox P., Roelfsema P. R., Baluteau J.-P., 2002a, *A&A*, 381, 606
- Martín-Hernández N. L., Vermeij R., Tielens A. G. G. M., van der Hulst J. M., Peeters E., 2002b, *A&A*, 389, 286
- Martins F., Plez B., 2006, *A&A*, 457, 637
- Martins F., Schaerer D., Hillier D. J., 2005, *A&A*, 436, 1049
- Mehring D. M., Goss W. M., Lis D. C., Palmer P., Menten K. M., 1998, *ApJ*, 493, 274
- Meynet G., Maeder A., Schaller G., Schaerer D., Charbonnel C., 1994, *A&AS*, 103, 97
- Moorwood A., Cuby J.-G., 1998, *The Messenger*, 94, 7
- Morisset C., Schaerer D., Bouret J.-C., Martin s F., 2004, *A&A*, 415, 577
- Morisset C., Schaerer D., Martín-Hernández N. L., Peeters E., Damour F., Baluteau J.-P., Cox P., Roelfsema P., 2002, *A&A*, 386, 558
- Morris P. W., van der Hucht K. A., Crowther P. A., Hillier D. J., Dessart L., Williams P. M., Willis A. J., 2000, *A&A*, 353, 624
- Okamoto Y. K., Katata H., Yamashita T., Miyata T., Sako S., Takubo S., Honda M., Onaka T., 2003, *ApJ*, 584, 368
- Pauldrach A. W. A., Hoffman T. L., Lennon M., 2001, *A&A*, 375, 161
- Peeters E., Martín-Hernández N. L., Damour F., et al. 2002, *A&A*, 381, 571
- Pérez-Montero E., Vílchez J. M., 2009, *MNRAS*, 400, 1721
- Pindao M., Schaerer D., González Delgado R. M., Stasińska G., 2002, *A&A*, 394, 443
- Quiroza C., Rood R. T., Balser D. S., Bania T. M., 2006, *ApJS*, 165, 338
- Reid M. J., 1993, *ARA&A*, 31, 345
- Rigby J. R., Rieke G. H., 2004, *ApJ*, 606, 237
- Rubin R. H., Simpson J. P., Colgan S. W. J., et al. 2007, *MNRAS*, 377, 1407
- Sellmaier F. H., Yamamoto T., Pauldrach A. W. A., Rubin R. H., 1996, *A&A*, 305, L37
- Sewilo M., Watson C., Araya E., Churchwell E., Hofner P., Kurtz S., 2004, *ApJS*, 154, 553
- Simón-Díaz S., Herrero A., Esteban C., Najarro F., 2006, *A&A*, 448, 351
- Simón-Díaz S., Stasińska G., 2008, *MNRAS*, 389, 1009
- Simpson J. P., Witteborn F. C., Price S. D., Cohen M., 1998, *ApJ*, 508, 268
- Stasińska G., Leitherer C., 1996, *ApJS*, 107, 661
- Storey P. J., Hummer D. G., 1995, *MNRAS*, 272, 41
- Thornley M. D., Schreiber N. M. F., Lutz D., Genzel R., Spoon H. W. W., Kunze D., Sternberg A., 2000, *ApJ*, 539, 641
- Vacca W. D., Johnson K. E., Conti P. S., 2002, *AJ*, 123, 772
- van Dishoeck E. F., 2004, *ARA&A*, 42, 119
- Verma A., Lutz D., Sturm E., Sternberg A., Genzel R., Vacca W., 2003, *A&A*, 403, 829
- Vermeij R., Damour F., van der Hulst J. M., Baluteau J.-P., 2002, *A&A*, 390, 649
- Vílchez J. M., Pagel B. E. J., 1988, *MNRAS*, 231, 257
- Vink J. S., de Koter A., Lamers H. J. G. L. M., 2001, *A&A*, 369, 574
- Watson A. M., Hanson M. M., 1997, *ApJ*, 490, 165
- Werner M. W., Roellig T. L., Low F. J., et al. 2004, *ApJS*, 154, 1
- Wood D. O. S., Churchwell E., 1989, *ApJS*, 69, 831
- Zhu Q.-F., Lacy J. H., Jaffe D. T., Richter M. J., Greathouse T. K., 2008, *ApJS*, 177, 584
- Zinnecker H., Yorke H. W., 2007, *ARA&A*, 45, 481